NUCL SCI TECH (2021) 32:65
https://doi.org/10.1007/s41365-021-00890-2

# The development, performances and applications of the monochromatic X-rays facilities in (0.218–301) keV at NIM, China

Si-Ming Guo[1] · Jin-Jie Wu[1] · Dong-Jie Hou[1]

Received: 15 March 2021 / Revised: 31 March 2021 / Accepted: 16 April 2021 / Published online: 23 June 2021


**Abstract** Space scientific exploration is rapidly becoming the primary battlefield for humankind to explore the universe. Countries worldwide have launched numerous space exploration satellites. Accurate calibration of the detectors on the ground is a crucial element for space science satellites to obtain observational results. For the purpose of providing calibration for various satellite-borne detectors, multiple monochromatic X-rays facilities have been built at the National Institute of Metrology, P.R. China (NIM). These facilities mainly pertain to grating diffraction and Bragg diffraction, and the energy range of the produced monochromatic X-rays is 0.218–301 keV. These facilities have a high performance in terms of energy stability, monochromaticity, and flux stability. The monochromaticity was greater than 3.0%. The energy stability of the facility is 0.02% at 25 keV over 8 h, and the flux stability was within 1.0% at 25 keV over 8 h. Calibration experiments on the properties of satellite-borne detectors, such as energy linearity, energy resolution, detection efficiency, and temperature response, can be conducted at the facilities. Thus far, the calibration of two satellites has been completed by the authors, and the work on three other satellites is in progress. This study will contribute to the advancement of X-ray astronomy the development of Chinese space science.

This work was supported by the National Key R&D Plan of China (2016YFF0200802) and Establishment of a standard device for air kerma in mammography X-rays (ANL1902).

✉ Jin-Jie Wu
gsm@nim.ac.cn; wujj@nim.ac.cn

1 National Institute of Metrology, Beijing, China

**Keywords** Monochromatic X-rays · Monochromator · Bragg diffraction · Energy spectra · Calibration

## 1 Introduction

The use of rockets or high-altitude balloons and other vehicles began in the 1960s; it was also when collimating scintillation crystals or gas detectors were employed to realize space X-ray detection. This marked the start of space astronomical observation research. X-ray astronomy largely involves the study of high-energy radiation celestial bodies through X-ray observation. The main observation objects include black holes, neutron stars, as well as interstellar high-temperature hot gases. Studies in this field largely focus on physical processes under extreme conditions such as extremely high density, extremely strong magnetic fields, and extremely strong gravitational fields. Between 2000 and 2014, the USA launched a total of 84 space exploration satellites, accounting for 27.6% of the total number of satellites launched worldwide. In 2017, the first Chinese space science satellite Hard X-ray Modulation Telescope (HXMT) was successfully launched, relaying significant research data [1, 2]. Presently, China has numerous space science satellites under development or are ready to be launched; examples include the gravitational wave high-energy electromagnetic counterpart all-sky monitor (GECAM) [3], hard X-ray imager (HXI) [4], space variable objects monitor (SVOM) [5, 6], and the enhanced X-ray timing and polarimetry mission (eXTP) [7]. The detectors utilized by many space science satellites are integral to space observations. Key parameters such as energy resolution, detection efficiency, and uniformity of these detectors must be ensured through ground calibration.

Otherwise, the inversion from observation data to real astronomical objects cannot be realized. Hence, research on monochromatic X-ray calibration facilities and calibration methods for detectors is required. There are several methods to produce monochromatic X-rays, namely radionuclides, synchrotron radiation, K fluorescence, and Bragg diffraction. Although radioactive sources are broadly used in detector calibration, their energy values are constant, rare, and uncontrollable. The synchrotron X-ray source is extensively used in a variety of fields, but it has the disadvantages of high cost, inconvenient application, and instability. K fluorescent X-rays are generated by primary X-rays to excite the secondary target. Owing to material restrictions, they are limited to a specific energy. Based on the continuous spectrum from an X-ray machine, monochromatic X-rays can be obtained through Bragg diffraction, whose energy is continuous and can be adjusted using different crystals and by altering the Bragg angle. This method is convenient, effective, and low cost for the application of detector performance calibration.

Internationally, monochromatic X-ray radiation facilities predicated on X-ray machines include the SOLEX device from the Becquerel laboratory in France [9–11], XACT in Italy [12], XRCF in the USA [13] and PANTER in Germany [14]; the main performance comparison between them is shown in Table 1. Satellites calibrated by these facilities include BeppoSAX [15], INTEGRAL/JEM-X [16], AXAF [17], Swift [18], and GBM [19, 20]. With regard to China, the HXCF [21] was jointly built by the National Institute of Metrology (NIM) of People's Republic of China and the Institute of High Energy Physics, Chinese Academy of Sciences. The energy range was 15–168 keV. The said facilities provide on-ground calibrations on energy linearity, energy resolution, detection efficiency, energy response matrix, and effective area of China's first astronomical satellite, HXMT [22], which laid the foundation for future scientific achievements [1, 23].

Detectors carried by space satellites form the core of space observation. Parameters such as the energy resolution, detection efficiency, and uniformity of these detectors must be calibrated on the ground. Otherwise, it is impossible to realize inversion from observation data to real astronomical phenomena. Therefore, it is necessary to develop monochromatic X-ray calibration devices and detector calibration methods. At present, research on monochromatic X-ray facilities in hard X-ray sections has achieved considerable research results and applications. In view of the shortcomings of monochromatic X-ray measurements and detector calibration in the soft X-ray energy section, combined with the demand for future space science development in China, we study monochromatic X-ray facilities in (0.218–301) keV to meet the demands for calibration of detectors. Owing to the large energy range, four sets of facilities were developed to realize monochromatic X-rays, and measurement research was also carried out. The theoretical calculation of the detection efficiency of the standard detector and experimental calibration under a standard radioactive source were completed. The measurement results were traced to the national primary standard for radionuclide activity. A traceability system of monochromatic X-ray flux in the energy range was established to ensure the accuracy and reliability of the applications. The research results will provide calibration services for space science satellite projects that have been established in China and data traceability support for next-generation space science satellites in space science planning in China. In addition, it could provide calibration support for the detectors used in dark matter research and

**Table 1** The emblematic monochromatic X-rays facilities in the world

| No. | 1 | 2 | 3 | 4 | 5 | 6 |
|---|---|---|---|---|---|---|
| Facility | XACT | XRCF | SOLEX | PANTER | Ferrara | HXCF |
| Country | Italy | USA | France | Germany | Italy | China |
| Energy (keV) | 0.1–30 | 0.09–10 | 1–20 | 0.25–50 | 15–140 | 20–161 |
| Flux ($cm^{-2}$ $s^{-1}$) | $10^5$ | – | $10^3$ | $10^4$ | – | $10^3$ |
| Spot size, φ (cm) | 0.1 | 400 | 0.035 | 100 | 0.5 | 0.5 |
| Beam length (m) | 35 | 518 | 0.5 | 120 | 100 | 6 |
| Clean room | Y | Y | Y | Y | Y | N |
| Vacuum | Y | Y | Y | Y | Y | N |
| Monochromator | Optical grating | Optical grating & DCM (Double-Crystal Monochromator) | SCM (Single-Crystal Monochromator) | Optical grating & DCM | DCM | DCM |
| Monochromaticity | – | < 1% | – | 4% at 10 keV | 1.7% at 17 keV | < 1% at 60 keV |

gravitational wave detection research and may promote China's breakthroughs in the frontier scientific area. This research achievement may support the development of space astronomy in China and enhance Chinese international competitiveness in X-ray astronomy.

## 2 Methods and experiment setup

For building monochromatic X-ray facilities to provide calibration and research conditions for space science satellite–borne detectors and other detectors, much research has been conducted at NIM, and several facilities have been come up. To date, (0.218–301) keV monochromatic X-rays generated by the facilities have been completed. The (0.218–1.6) keV monochromatic X-rays are generated by X-ray machines and diffracted by gratings, whereas a (5–301) keV energy range is produced using the Bragg diffraction of crystals.

### 2.1 The (0.218–1.6) keV X-ray facility

The (0.218–1.6) keV monochromatic X-ray beam facility predominantly consists of an X-ray machine, a non-harmonic grating monochromator, and a detector. The Bremsstrahlung radiation spectrum generated by the X-ray machine enters the non-harmonic monochromator to achieve dispersion focusing, upon which the adjustable monochromatic X-ray beam is obtained at the exit. The source is a customized multi-target windowless X-ray machine (WORX, model XWT-065-SE) with five target materials. The structure is illustrated in Fig. 1.

Considering the convenience and stability provided by the focused light source, the monochromator is directly connected to the source without a front-focusing system. The non-harmonic grating monochromator adopts the CT optical structure and employs two toroidal mirrors to realize collimation and focusing functions. The focus positions are at the entrance and exit of the slit. The incident and diffracted beams of the grating are parallel in the spectral resolution direction. During wavelength scanning, only one element of the grating needs to be rotated, and the focusing conditions can be met without moving the exit slit.

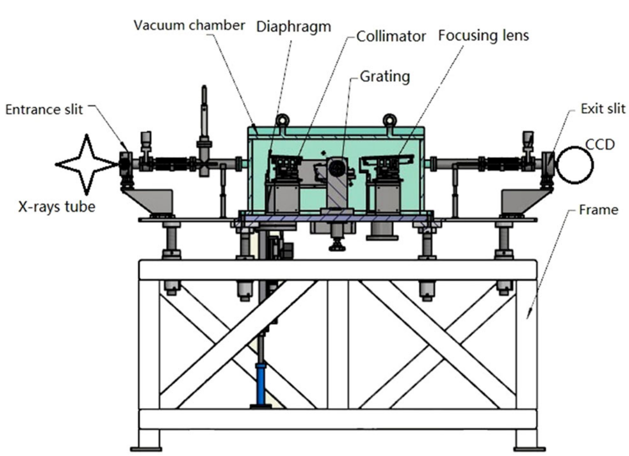


**Fig. 1** (Color online) Schematic configuration of the soft X-ray monochromator

Characteristic X-rays corresponding to different target materials can be generated when the target materials are changed. The main parameters of the X-ray machine and monochromator are listed in Table 2.

The monochromator could produce (218–1600) eV monochromatic X-rays; if the Bragg diffraction crystal is used to generate the monochromatic X-rays, the energy range may be larger. Because the X-tube is multi-target, it could produce stable characteristic peaks of the targets, such as Si, $K_{\alpha1}$: 1.74 keV, $K_{\alpha2}$: 1.739 keV, $K_{\beta1}$: 1.832 keV, Ti, $K_{\alpha}$: 4.5 keV, $K_{\beta}$: 4.93 keV, $L_{\alpha}$: 0.452 keV, $L_{\beta}$: 0.458 keV, Ag, $L_{\alpha1}$: 2.984 keV, $L_{\alpha2}$: 2.978 keV, $L_{\beta1}$: 3.151 keV, $L_{\beta2}$: 3.384 keV, $L_{\gamma}$: 3.519 keV.

### 2.2 The (5–40) keV X-ray facility

The (5–40) keV monochromatic X-ray beam facility is principally composed of an X-ray machine, a diffraction crystal, and a synchronous rotating device. The monochromator comprises a high-precision rotator and a Bragg diffraction crystal, with monochromatic X-rays producing and passing through the monochromator. The process follows Bragg's law [24]:

$$2d\sin\theta = n\lambda, \tag{1}$$

where $d$ is the crystal constant, $n$ is the diffraction series, $\theta$ is the Bragg's angle, and $\lambda$ is the wavelength. According to Eq. (2), the energy of monochromatic X-rays can be deduced as follows:

$$E = hv, c = \lambda v \Rightarrow E = \frac{nhc}{2d\sin\theta}. \tag{2}$$

The uncertainty of the photon flux introduced by the position uncertainty is substantially large, and a position deviation of 1 mm may cause a 20% flux error; furthermore, the position accuracy is critical for the detection efficiency calibration of the detector. The double-crystal monochromator is advantageous in that there is only a slight translation in the X-ray emission direction when different energies are adjusted, and no angular deflection occurs. This is beneficial to the detection efficiency calibration. In contrast, the single-crystal monochromator has an energy corresponding to an angle. Every time the energy is changed, the angle needs to be adjusted; thus, every angle change alters the position of the detector, introducing

**Table 2** The first instrument characteristics

| X-ray tube | | Monochromator | |
|---|---|---|---|
| Anode voltage | 5–30 kV | Energy range | 218–1600 eV |
| Max anode current | 5 mA at 10 kV | Incident angle range | 85.6°–88.6° |
| Focal spot size (nominal) | 20 μm-200 μm | Monochromaticity | $\Delta E/E < 2.5\%$ |
| Anode material | Si, Cu, Ti, Ag, Cr | Higher harmonic | $< 0.3\%$ |
| Cooling method | Water | Adjustable step | $< 10$ eV |
| Flux stability | better than ± 0.5% | Vacuum degree | $\leq 5 \times 10^{-4}$ Pa |
| Flux linear | better than ± 0.5% | Divergence angle | $\geq 5$ mrad × 10 mrad |
| Continuous working period | $\geq 10$ h | Grating line width | 1500 lp/mm |

a considerable amount of uncertainty. The best method to address this issue involves fixing the direction of the X-ray emissions, with no need to alter the position of the detector when adjusting different energies. To guarantee that the direction of the X-ray emissions remains unchanged, the design scheme adopted is as shown in Fig. 2.

The monochromator was separately placed on a turntable; the monochromator and the tube were also placed on the same platform, and the upper and lower rotations were controlled by two motors. The upper motor controls the rotation of the crystal and the lower motor controls the X-ray machine. When the crystal rotates at an angle $\theta$, the X-ray machine rotates at an angle of $2\theta$ to ensure that the direction of the monochromatic X-rays does not change. The detailed parameters are listed in Table 3

### 2.3 The (20–161) keV X-ray facility

The (20–161) keV X-ray facility comprises an X-ray tube, monochromator, detector, and control system, as depicted in Fig. 3. The X-ray continuous spectrum emitted by the X-ray tube subsequently impacts the double-crystal monochromator. The crystal alters the angle under the control of a high-precision turntable and T structure, and monochromatic X-rays are produced. Monochromatic X-rays are ultimately detected after passing through the collimator and the beam-limiting aperture.

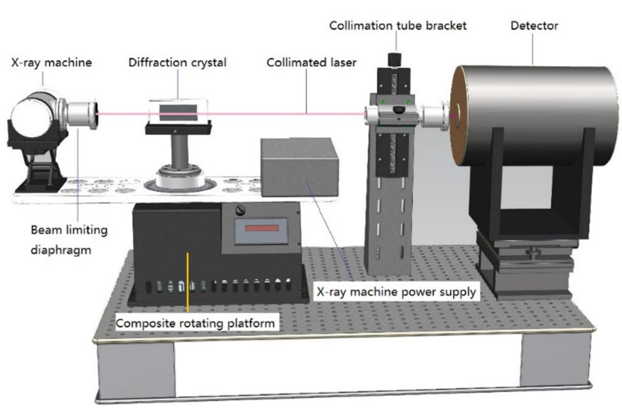


**Fig. 2** (Color online) Schematic configuration of the (5–40) keV monochromatic X-rays beam facility

The double-crystal monochromator is an X-ray diffraction device with high precision and resolution, utilizing the Bragg diffraction law for crystals, and includes a double-crystal, high-precision rotator, T structure, beam regulator, and aperture. The principle of the structure is shown in Fig. 3. The monochromator employs two parallel crystals as the original dispersion; the first crystal ("crystal I") realizes monochromaticity. Under the action of the fixed height difference structure, the second crystal ("crystal II") maintains the exit direction and height of the output monochromatic light relative to the incident light, so as to obtain a light spot with a fixed position. Detailed parameters are listed in Table 4.

### 2.4 The (21–301) keV X-ray facility

The configuration of the (21–301) keV X-ray facility is illustrated in Fig. 4. Owing to the limitation of the structure of the double-crystal monochromator, higher-energy monochromatic X-rays cannot be generated by the diffraction of a double-crystal monochromator. Single-crystal monochromators have, therefore, become a better choice. The Bragg angle can be adjusted by controlling the rotator, and thus, different monochromatic X-rays can be generated.

The X-ray machine utilizes the Y.MG605 type X-ray machine of YXLON Company, with a rated voltage range of 20–600 kV. The detailed parameters are listed in Table 5.

## 3 Performance test and results

### 3.1 Detectors

#### *3.1.1 HPGe*

A high-purity germanium (HPGe) detector (GL0110) was chosen as the first standard. Combined with the

**Table 3** The second instrument characteristics

| X-ray tube | | Monochromator | |
|---|---|---|---|
| Max anode voltage | 15 kV-50 kV | Energy range | 5–40 keV |
| Max anode current | 1 mA at 50 kV | Bragg angle | 4°–25° |
| Max filament current | 1.7 A | Monochromaticity | $\Delta E/E < 3\%$ at 10 keV |
| Focal spot size (nominal) | 110 μm | Monochromatic light | $> 90\%$ |
| Anode material | Cu | Flux | $> 5000$ cm$^{-2}$ s$^{-1}$ |
| Be window thickness | 125 μm | Adjustable step | $< 0.2$ keV |
| Stability | 0.2% over 4 h | Spot size, φ | 1–10 mm |
| Cooling method | Water | Single crystal | LiF(220), LiF(420), Ge(111) |

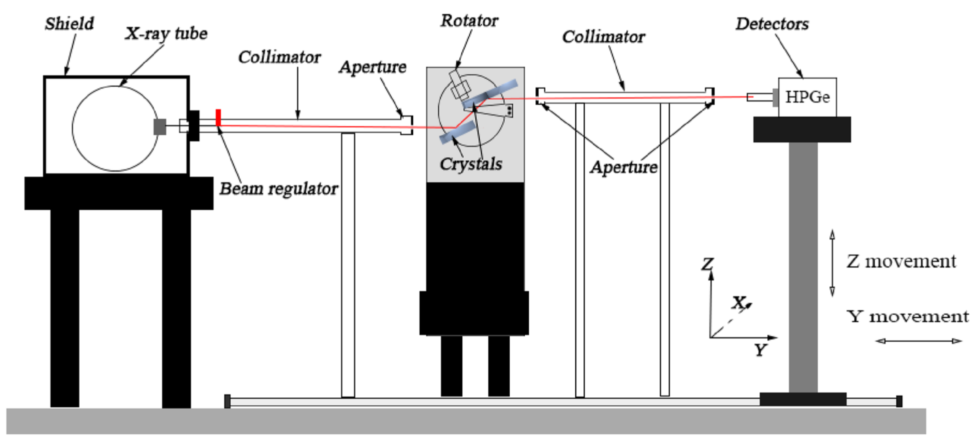


**Fig. 3** (Color online) Schematic configuration of the (20–161) keV monochromatic X-rays beam facility

**Table 4** The third instrument characteristics

| X-ray tube | | Monochromator | |
|---|---|---|---|
| Anode voltage | 10–225 kV | Energy range | 20–161 keV |
| Max anode current | 60 mA at 40 kV | Bragg angle | 2.5°–7.5° |
| Max filament current | 4.2 A | Monochromaticity | $\Delta E/E < 2\%$ at 60 keV |
| Focal spot size (nominal) | 0.4 mm or 3 mm | Monochromatic light | $> 90\%$ |
| Anode material | W | Flux | $> 2000$ cm$^{-2}$ s$^{-1}$ |
| Be window thickness | 800 μm | Adjustable step | $< 0.2$ keV |
| Stability | 0.1% over 4 h | Spot size, φ | 1–10 mm |
| Cooling method | Water | Double crystal | Si(220), Si(551) |

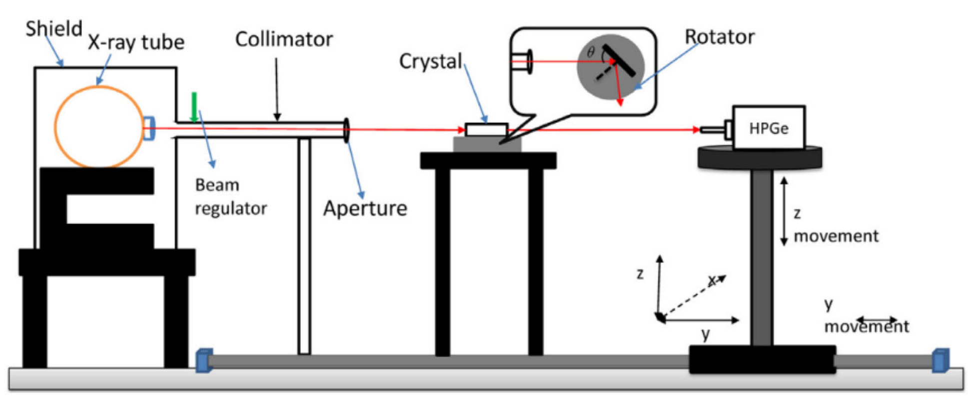


**Fig. 4** (Color online) Schematic configuration of the high-energy facility

parameters provided by the manufacturer, the internal structure of the detector is obtained by industrial CT scanning, the geometric model is established to simulate the detection efficiency by Monte Carlo (MC) codes, and

**Table 5** The fourth instrument characteristics

| X-ray tube | | Monochromator | |
|---|---|---|---|
| Max anode voltage | 20–600 kV | Energy range | 21–301 keV |
| Max anode current | 7.5 mA at 200 kV | Bragg angle | 1.5°–25° |
| Max filament current | 3.7 A | Monochromaticity | $\Delta E/E < 3\%$ |
| Focal spot size (nominal) | 0.5 mm or 1.5 mm | Monochromatic light | $> 90\%$ |
| Anode material | W | Flux | $> 2000\ \text{cm}^{-2}\ \text{s}^{-1}$ |
| Window thickness | 2 mm Be and 3 mm Al | Adjustable step | $< 1$ keV |
| Stability | 0.3% over 4 h | Spot size, φ | 1–10 mm |
| Cooling method | Oil | Single crystal | Si(220), Si(551) |

the point source extrapolation experiment was verified before the detection efficiency of the HPGe was finally obtained. A perspective image of the HPGe is shown in Fig. 5.

An experimental calibration was conducted, as shown in Fig. 6. Three radioactive sources, $^{241}$Am, $^{57}$Co, and $^{109}$Cd, were selected for the experiment. Upon calculation of the experimental data, the experimental efficiencies at different energies were obtained. Specific experimental methods are provided in Ref. [25].

On comparing the simulation and experiments [26], the results were determined to fit well after necessary corrections were met. The results are presented in Table 6.

The HPGe detection efficiency curves are shown in Fig. 7. The test data points in the figure were measured by experiments pursuant to the point source extrapolation method. The curve is calculated by establishing a Monte Carlo model based on the CT scan image of the HPGe detector and is used for the beam flux calculation.

*3.1.2 SDD*

A silicon drift detector (SDD) is another standard detector. Owing to its high performance, the said detector has been extensively used in scientific research. The detection area is 20 mm$^2$, its length is 450 µm, the thickness of incident beryllium window is 8 µm, and the FWHM is greater than 133 eV at 5.9 keV.

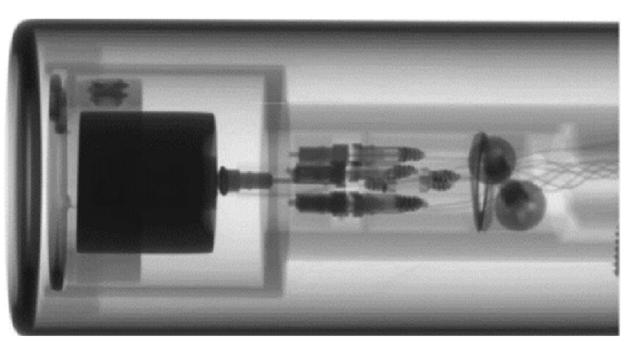

**Fig. 5** The CT image of the detector

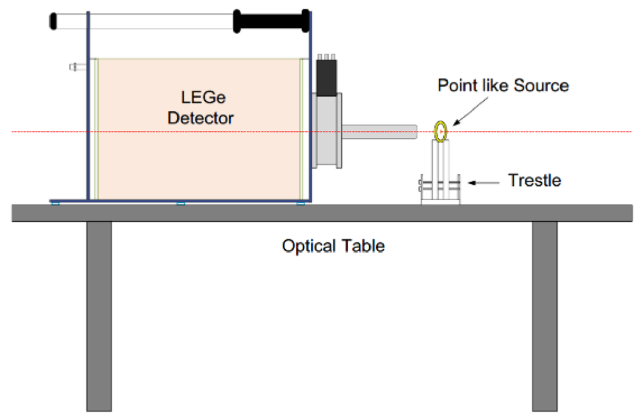


**Fig. 6** (Color online) Calibration experiment

The detection efficiency was determined by calculating the response of the detector to different incident energy photons using MC simulation software, and then the reliability of the calculation results is verified using the known activity of the radioactive source for calibration experiments. The structure data of the detector used in the calculation mainly refer to the factory instructions and industrial CT scanning results. The structure used in the simulation is shown in Fig. 8.

The simulation results show that the detection efficiency of the SDD is excellent below 10 keV, and the detection efficiency decreases rapidly with an increase in energy (Fig. 9).

*3.1.3 CCD*

Two CCD cameras were used. One was PIXIS-XF 2048 B. It has excellent performance in radiation detection owing to the 2048 × 2048 array and the rapid measurement system. The other CCD was from Andor DO934P-BN; the imaging array used was 1024 × 1024, the pixels were 13 µm × 13 µm, and the maximum speed was 5 MHz. The detection efficiency of the two cameras is shown in Fig. 10.

**Table 6** Results from simulation and experiments

| Energy (keV) | Experimental intrinsic full-energy peak efficiency (%) | Simulation intrinsic full-energy peak efficiency (%) | *RD* (%) |
|---|---|---|---|
| 14.41 | 87.6(15) | 87.8(9) | − 0.28 |
| 22.08 | 92.9(10) | 93.29(10) | − 0.47 |
| 59.54 | 97.8(9) | 98.38(10) | – 0.52 |
| 88.03 | 94.6(11) | 94.81(10) | 0.04 |
| 122.06 | 72.6(9) | 73.88(9) | − 1.8 |
| 136.47 | 63.4(10) | 63.35(8) | 0.07 |

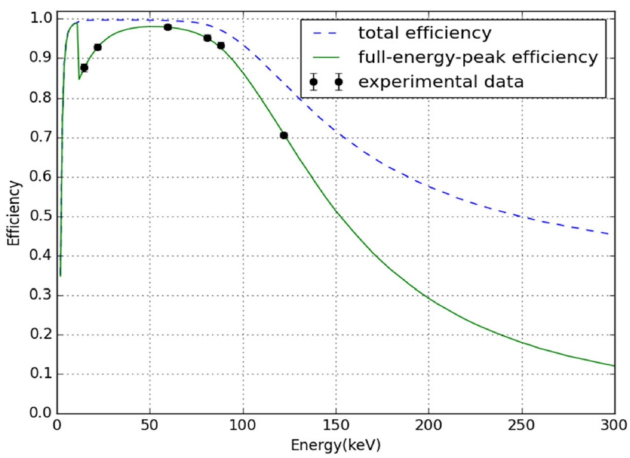


**Fig. 7** The detection efficiency obtained from MC for parallel incident photons and experiment

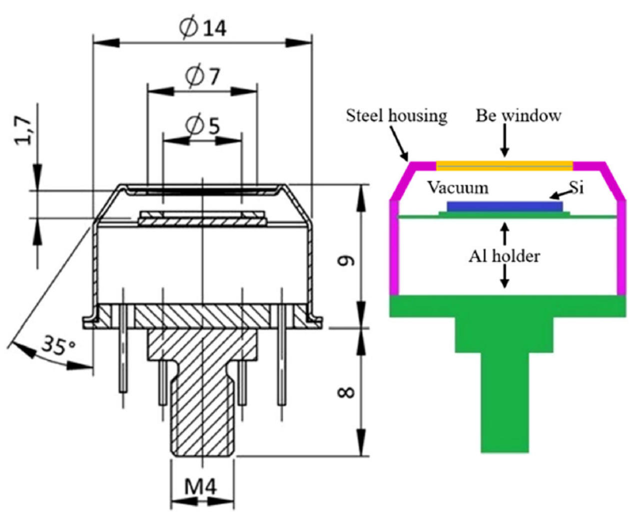


**Fig. 8** (Color online) The SDD structure

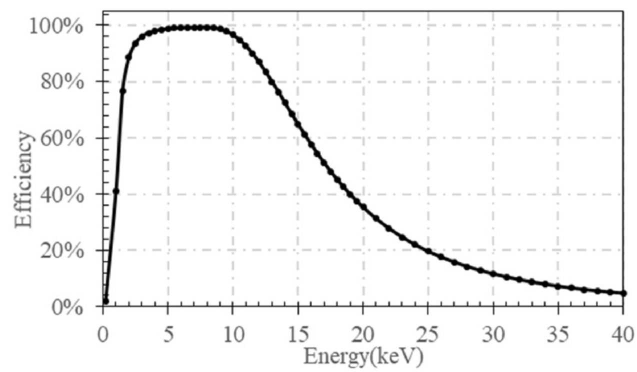


**Fig. 9** Calculated intrinsic efficiency of SDD

## 3.2 Data and discussion

### *3.2.1 Measurements of (0.218–1.6) keV photons*

The zero-order spot was recorded on the CCD detector when the grating was adjusted to the horizontal position. The position coordinates of the center point of the zero-order spot were (1318, 1092), and the incident angle was $\alpha$. The first-order spot was recorded while the grating angle was rotated to 949.8 eV ($\lambda$ = 1.305 nm). The position of the light spot center could be ultimately located in the zero-order coordinates (1318, 1092) by further rotating the grating angle slightly; at this point, $\Delta\alpha$ = 0.851°. Pursuant to grating diffraction equation

$$\sin(\alpha + \Delta\alpha) - \sin(\alpha - \Delta\alpha) = \lambda\rho. \tag{3}$$

Thus, from $\Delta\alpha$ and $\lambda$, the actual incident angle of the zero-order $\alpha$ = 87.0715° can be obtained. Subsequently, a first-order spot of 828 eV was collected on the CCD while the grating was rotated to 0.976°, as shown in Fig. 11.

After replacing the target with Ti and rotating the grating to 1.762°, the first-level spot of 458.3 eV was recorded by the CCD. When the grating was rotated, the limit of the rotation angle was 0.5052° and 3.7° for the 1500 lp/mm grating, and the corresponding energies were 1600 eV and 218 eV, respectively. Hence, the working energy range of the monochromator was 218–1600 eV. On

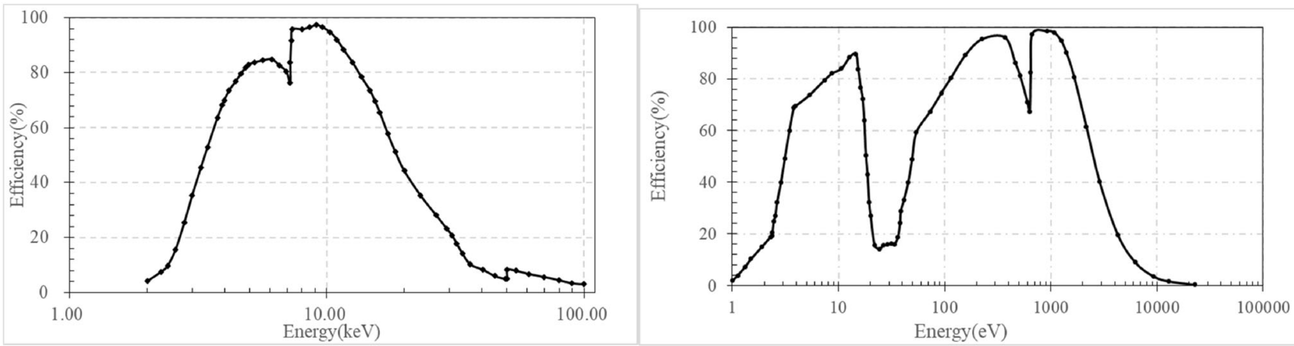


**Fig. 10** Detection efficiency of PXF:2048B (left) and DO934P-BN (right)

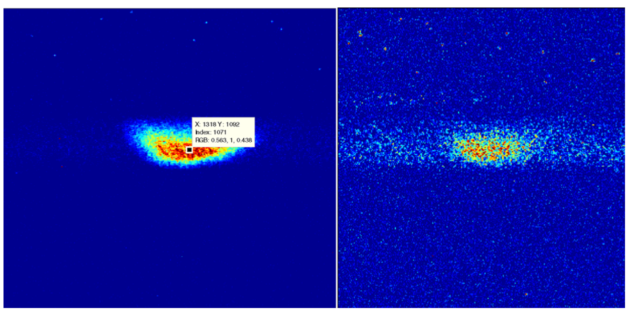

**Fig. 11** (Color online) Cu target X-ray source 949.8 eV primary spot (left) and 828 eV primary spot (right)

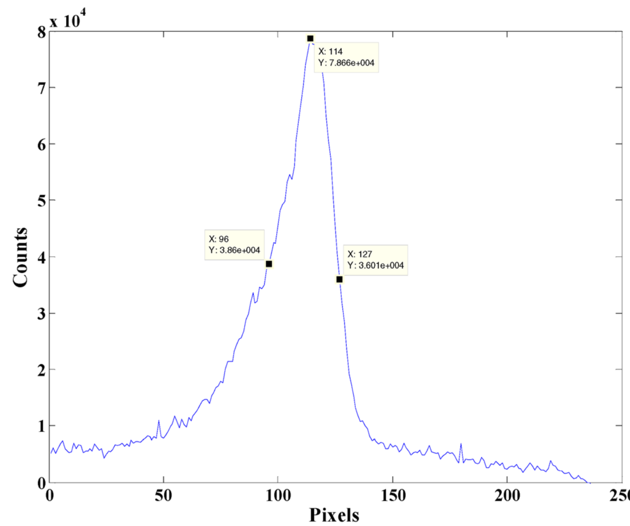


**Fig. 12** Experimental result of the 949.8 eV X-ray

the CCD detection surface, the spot length was 103 pixels (approximately 1.39 mm), and the spot height was 39 pixels (approximately 0.53 mm). The total photon count was $1.64 \times 10^6$/min, and hence, the count rate was $2.7 \times 10^4$ cps at 949.8 eV.

At the best resolution position of the first-level spot at 949.8 eV ($\lambda = 1.305$ nm), the grating incident angle was 87.0661°. The number of pixels for broadening the spectral lines, $\Delta N = 31$(FWHM), was acquired from the measured spot. Furthermore, the distance between the center of the CCD array and the focusing lens was $L = 800$ mm; hence, the angle broadening corresponding to the FWHM of the spectral line was calculated as $\Delta N \times 13.5$ μm/L $= 5.23 \times 10^{-4}$. In accordance with the grating equation:

$$\sin\alpha - \sin(\beta \pm 13.5\Delta N/(2L)) = (\lambda \mp \Delta\lambda_{\mp})/d. \quad (4)$$

Next, the energy broadening corresponding to the angular broadening $\Delta E = 20.496$ eV was obtained. Additionally, the energy resolution was obtained as $E/\Delta E \approx 46$ at 949.8 eV (2.2% at 949.8 eV), as shown in Fig. 12. The energy stability was better than 0.2% at 1 h, and the flux stability was within 0.5% at 1 h. Benefitting from the high precision of the vacuum turntable structure and a very stable X-ray generator, its stability was found to be excellent.

### 3.2.2 *Measurements of (5–40) keV X-rays*

The SDD detector was used to collect data every 30 min, and the energy stability was obtained through long-term measurement, thereby ensuring the stability of the device, as shown in Fig. 13.

The energy stability of the facility was 0.02% at 25 keV over 8 h, and the flux stability thereof was within 1.0% at 25 keV 8 h.

The energy range of the facility was determined experimentally, whereas the energy spectra were obtained using the SDD and HPGe detectors. A portion of the experimental results is shown in Fig. 14.

Photons are scattered after passing through a 3 mm beam limiting diaphragm, resulting in a spot size larger than the aperture of the diaphragm. The CCD detector was moved to the center of the laser position. The coordinates of the edge of the spot were measured as (739, 713), (1016, 713), (874, 551), and (874, 881). The image obtained by CDD measurement was 13.5 μm per pixel; thus, the

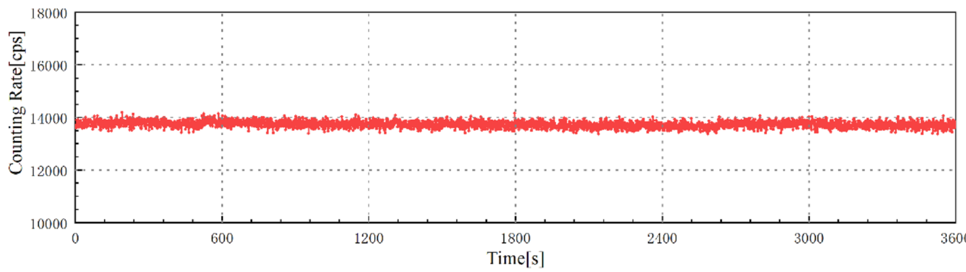


**Fig. 13** (Color online) The flux stability at 25 keV

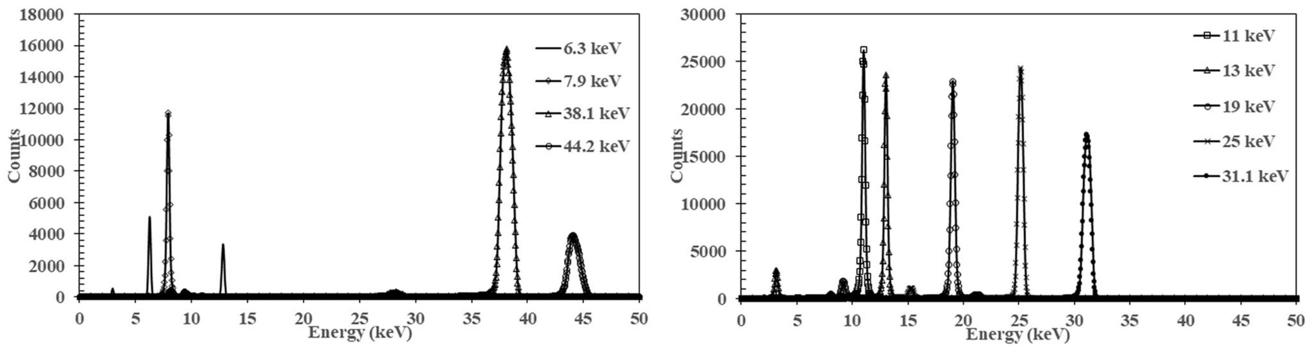


**Fig. 14** (Color online) The measured monochromatic spectra under LiF220 crystal monochromator

horizontal length of the spot was 3739.5 μm and the vertical length was 4455 μm, as shown in Fig. 15.

The HPGe detector was used to measure the performance of the device in more detail. The performance parameters, such as flux and monochromaticity, are listed in Table 7. In the present experimental mode, the minimum flux was greater than 5000 $cm^{-2}\ s^{-1}$. This value can be altered by adjusting the parameters of the X-ray machine. The monochromaticity was obtained by subtracting the energy resolution of the detector from the measurement results. The monochromaticity of the device in the measured energy range was below 3.24%, which is highly favorable and able to meet the calibration requirements of almost all detectors. The monochromaticity of the facility was then measured. Because the detector has energy resolution, the energy resolution of the measured all-round peak deducting the energy resolution of the detector itself is the monochromaticity of the monochromatic X-ray source.

### *3.2.3 Measurements of (20–161) keV X-rays*

In this study, the double-crystal monochromator could cover the energy range of 20–161 keV using Bragg diffraction crystals Si(220) and Si(551). Several spectra measured by HPGe were selected, and the double-crystal monochromator was rotated so that the maximum diffraction angle could reach the lower limit of the energy, and the minimum diffraction angle could obtain the maximum energy. Owing to the limitation of the structure, the rotation range of the double-crystal monochromator for different crystals would be slightly different, and the energy

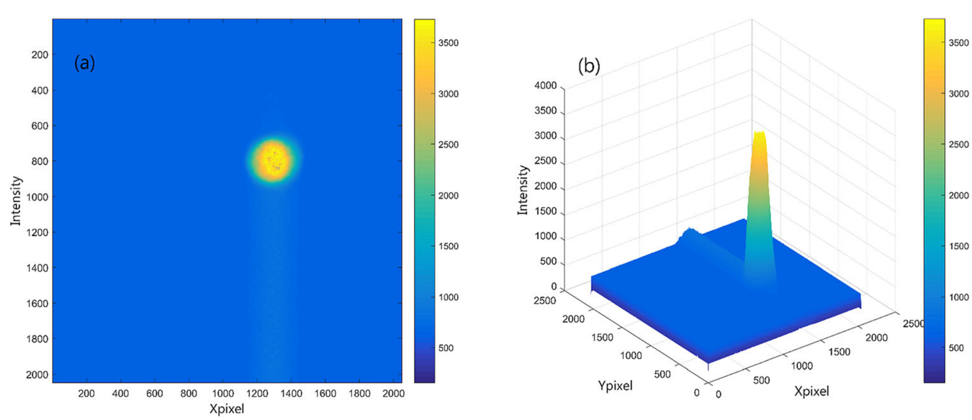


**Fig. 15** (Color online) Measurement of the spot distribution

**Table 7** The measurement results from the experiment

| Energy (keV) | Count rate (cps) | Efficiency | Flux ($cm^{-2}$ $s^{-1}$) | FWHM (keV) | Monochromaticity (%) |
|---|---|---|---|---|---|
| 6.3 | 353.29 | 0.968 | 5165.87 | 0.232 | 2.10 |
| 7.1 | 546.31 | 0.979 | 7898.49 | 0.292 | 3.11 |
| 7.9 | 956.86 | 0.981 | 13,805.98 | 0.295 | 2.84 |
| 9 | 1685.76 | 0.986 | 24,199.52 | 0.304 | 2.62 |
| 10 | 1905.9 | 0.983 | 27,443.18 | 0.306 | 2.38 |
| 11 | 2512.4 | 0.9897 | 35,931.31 | 0.327 | 2.40 |
| 12 | 2193.51 | 0.8557 | 36,283.23 | 0.331 | 2.24 |
| 13 | 2558.73 | 0.8657 | 41,835.49 | 0.337 | 2.12 |
| 14 | 2725.41 | 0.8752 | 44,077.03 | 0.352 | 2.10 |
| 15 | 1986.58 | 0.8841 | 31,804.79 | 0.365 | 2.06 |
| 16 | 1806.21 | 0.8926 | 28,641.73 | 0.379 | 2.03 |
| 19 | 2964.61 | 0.9151 | 45,855.02 | 0.43 | 2.01 |
| 22.1 | 2836.63 | 0.9329 | 43,038.33 | 0.46 | 1.88 |
| 25.1 | 3349.95 | 0.9466 | 50,091.00 | 0.554 | 2.06 |
| 28 | 3414.63 | 0.9568 | 50,513.83 | 0.667 | 2.27 |
| 31.1 | 3500.82 | 0.9646 | 51,370.09 | 0.83 | 2.59 |
| 34.1 | 3509.86 | 0.9705 | 51,189.64 | 0.99 | 2.84 |
| 37.1 | 3073.89 | 0.9735 | 44,693.07 | 1.149 | 3.05 |
| 38.1 | 4555.51 | 0.976 | 66,065.54 | 1.212 | 3.14 |
| 39 | 4105.2 | 0.977 | 59,474.06 | 1.266 | 3.20 |
| 40.1 | 3721.47 | 0.978 | 53,859.65 | 1.315 | 3.24 |
| 42.1 | 2400 | 0.9796 | 34,677.70 | 1.318 | 3.09 |
| 44.2 | 1182.65 | 0.9809 | 17,065.51 | 1.221 | 2.72 |

would also be limited because of the influence of the crystal length and the distance between the two crystals. In theory, although various crystals have a significantly wide energy range, the theoretical range will be reduced because of the limitation of the processing structure. Each crystal had an excellent flux and energy resolution within the appropriate energy range. The measured spectra are shown in Fig. 16.

The flux stability was measured after the X-ray tube was warmed. Here, the flux changes within 10 h were recorded under certain X-ray tube voltages and currents. Two sets per hour were recorded for each set for 1000 s. The flux stability was greater than 0.8% over 10 h (Fig. 17).

Under normal circumstances, a uniform spot with good monochromaticity was obtained at less than 10 mm. The size of the light plate primarily depends on the size of the beam-limiting diaphragm. A CCD detector was used to measure the light spot under a beam-limiting diaphragm with a diameter of 4 mm, as shown in Fig. 18.

The HPGe detector was used to measure the performance of the device in more detail. The performance parameters, such as flux and monochromaticity, are listed in Table 8. In the present experimental mode, the minimum flux was greater than 2000 $cm^{-2}$ $s^{-1}$. The monochromaticity was obtained by subtracting the energy resolution of the detector from the measurement results. The

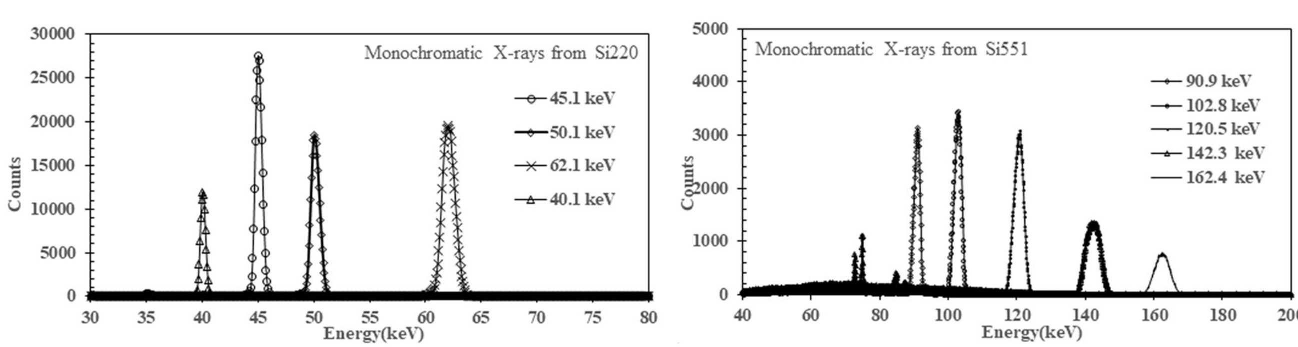


**Fig. 16** (Color online) The measured monochromatic spectra using a double-crystal monochromator

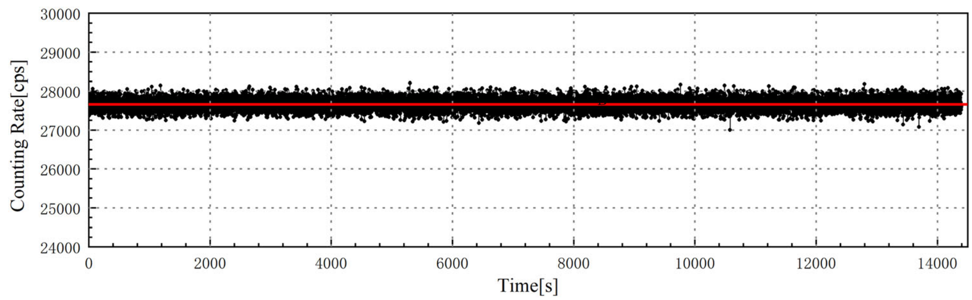


**Fig. 17** The flux stability at 127 keV

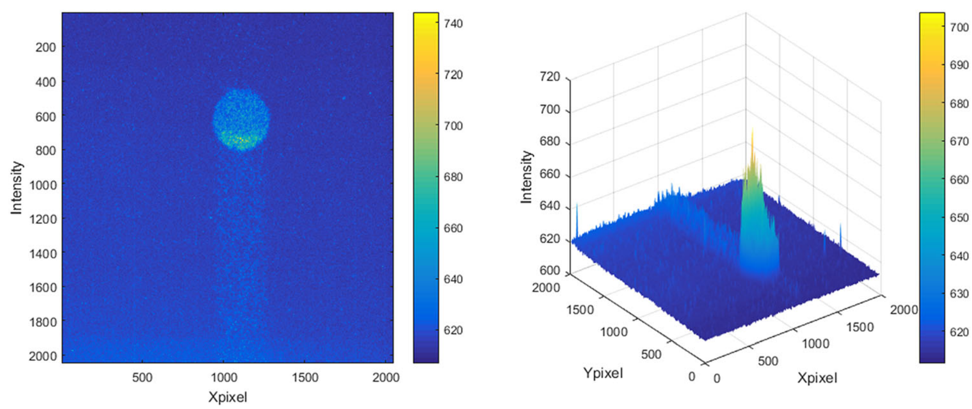


**Fig. 18** (Color online) Measurement of light spot

monochromaticity of the device in the measured energy range was below 3.55%.

### 3.2.4 *Measurements of (21–301) keV X-rays*

The monochromatic X-rays were measured using an HPGe detector, and the device was studied in detail. Several typical energy spectra are shown in Fig. 19. In fact, three Si crystals were used in the monochromator, and the generated monochromatic X-rays were related to different crystals. Ultimately, (21–301) keV was realized on this facility.

The detailed measurement parameters are listed in Table 9. The monochromaticity was better than 5.74%, whereas the minimum flux was greater than 2000 $cm^{-2}\ s^{-1}$. After detailed measurements, this facility was found to have good performance in terms of stability and a linear relationship between flux and cube current.

**Table 8** The specification of the double-crystal monochromator

| Energy (keV) | Count rate (cps) | Efficiency | Flux ($cm^{-2}\ s^{-1}$) | FWHM (keV) | Monochromaticity (%) |
|---|---|---|---|---|---|
| 37.9 | 344.07 | 0.97597 | 2806.86 | 0.489 | 1.06 |
| 39.1 | 602.35 | 0.97705 | 4908.43 | 0.521 | 1.12 |
| 40.1 | 872.71 | 0.97797 | 7104.85 | 0.548 | 1.16 |
| 45.1 | 2588.1 | 0.98144 | 20,995.57 | 0.708 | 1.41 |
| 50.1 | 2243.61 | 0.98324 | 18,167.63 | 0.909 | 1.69 |
| 62.1 | 3439.53 | 0.98374 | 27,837.43 | 1.342 | 2.08 |
| 70.1 | 691.32 | 0.98116 | 5609.83 | 1.263 | 1.71 |
| 80.6 | 344.48 | 0.96899 | 2830.45 | 1.619 | 1.94 |
| 90.9 | 808.39 | 0.93955 | 6850.33 | 2.062 | 2.21 |
| 102.8 | 1116.09 | 0.87914 | 10,107.68 | 2.572 | 2.46 |
| 111.5 | 946.76 | 0.82555 | 9130.76 | 2.879 | 2.54 |
| 120.5 | 1271.27 | 0.75899 | 13,335.59 | 3.271 | 2.68 |
| 130.5 | 941.63 | 0.68695 | 10,913.54 | 3.982 | 3.02 |
| 142.3 | 874.2 | 0.60111 | 11,578.90 | 5.081 | 3.55 |
| 151.7 | 790.42 | 0.54215 | 11,607.77 | 5.381 | 3.53 |
| 162.4 | 526.63 | 0.48178 | 8702.96 | 5.162 | 3.16 |

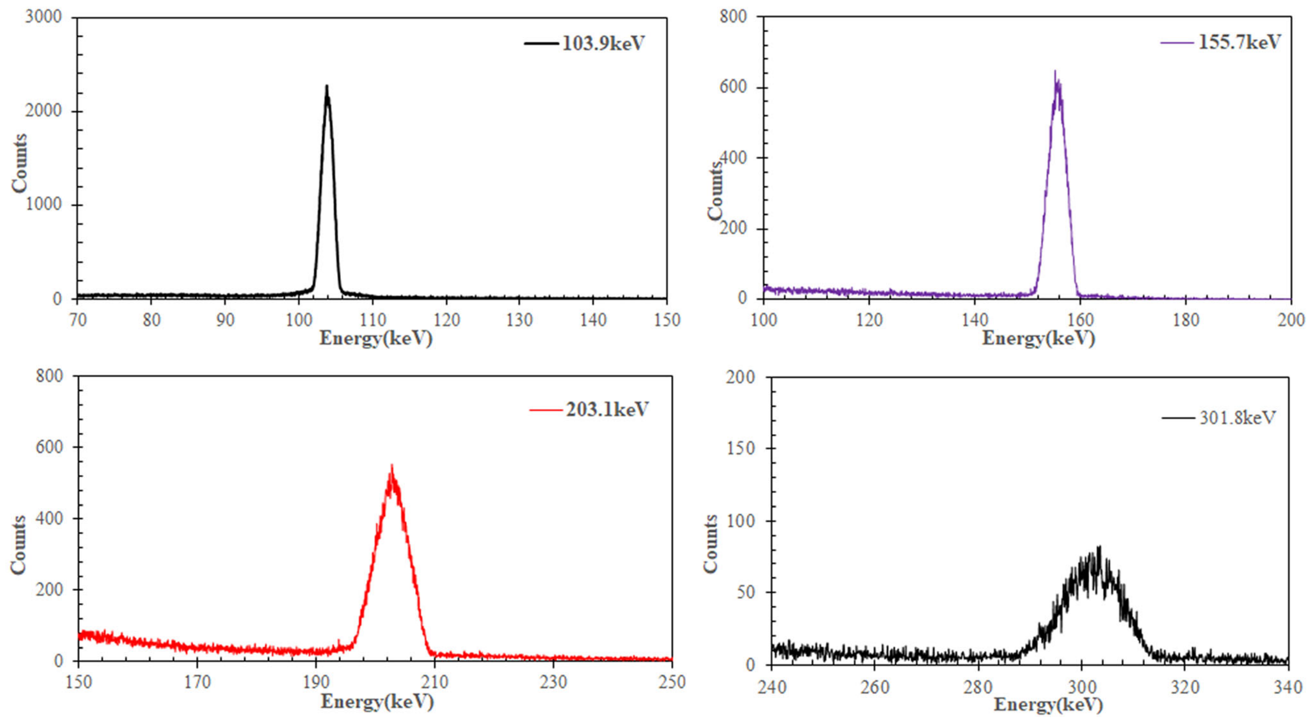


**Fig. 19** (Color online) The measured monochromatic spectra under Si(551) crystal

The energy stability was better than 0.4% within 50 h, whereas the flux stability was better than 1.4% within 50 h. The said facility can be used to conduct X-ray diffraction studies and detector calibration studies.

## 4 Applications

In recent years, several space science projects related to X-ray detection have been developed in China. Insight-HXMT was completed in 2017. High-energy detectors are the main components of the HXMT payload. The main detectors and backup detectors thereof have completed calibration of energy linearity, detection efficiency, and energy resolution on the present calibration device, and the energy range covers (20–150) keV [27]. The experimental energy resolution of the HED Z01-25 detector is shown in Fig. 20. The calibrated detection efficiencies of all 24 detectors at the present facility are presented in Fig. 21. The experimental calibration results verified the detection efficiency of the theoretical calculations.

**Table 9** The specification of the high-energy monochromator

| Energy (keV) | Count rate (cps) | Efficiency | Flux ($cm^{-2}$ $s^{-1}$) | FWHM (keV) | Monochromaticity (%) |
|---|---|---|---|---|---|
| 51.9 | 365.5 | 0.9838 | 2957.95 | 0.565 | 0.73 |
| 93.6 | 1018.56 | 0.9292 | 8727.46 | 1.585 | 1.63 |
| 103.7 | 1079.68 | 0.8765 | 9807.39 | 1.924 | 1.80 |
| 116.8 | 1038.8 | 0.7856 | 10,527.88 | 2.35 | 1.97 |
| 155.7 | 578.97 | 0.5232 | 8810.46 | 3.828 | 2.44 |
| 186.6 | 845.07 | 0.3707 | 18,150.16 | 5.464 | 2.92 |
| 203.1 | 789.38 | 0.3123 | 20,124.47 | 6.039 | 2.96 |
| 232.5 | 505.23 | 0.2352 | 17,102.60 | 7.675 | 3.29 |
| 251.4 | 255.15 | 0.2001 | 10,152.17 | 7.542 | 2.99 |
| 258.4 | 360.74 | 0.1887 | 15,220.63 | 7.548 | 2.91 |
| 266.2 | 195.85 | 0.1769 | 8814.67 | 8.646 | 3.24 |
| 301.5 | 103.83 | 0.1372 | 6025.31 | 6.77 | 2.24 |
| 302.8 | 90.58 | 0.1358 | 5310.59 | 6.905 | 2.27 |
| 310.2 | 252.05 | 0.1266 | 15,851.24 | 17.8 | 5.74 |

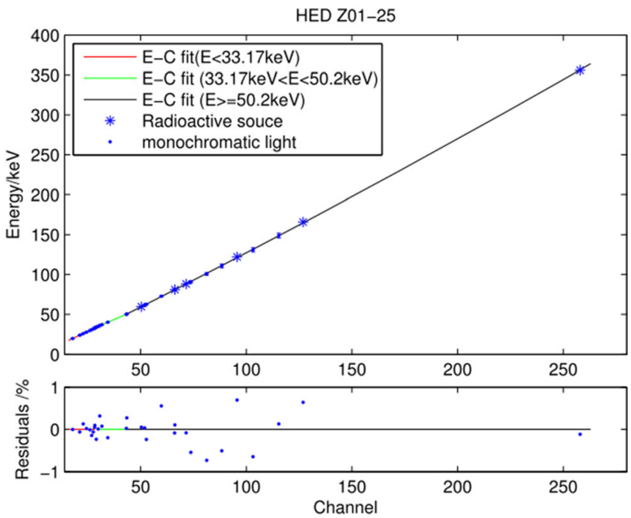


Fig. 20 (Color online) EC relations for a NaI detector

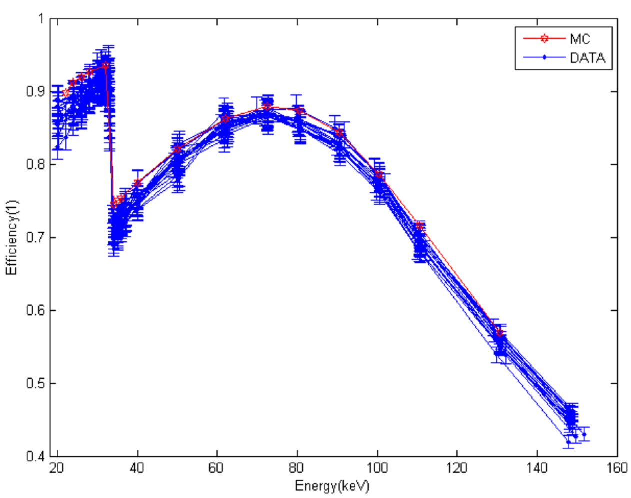


Fig. 21 (Color online) Detection efficiency experiments and MC calculation

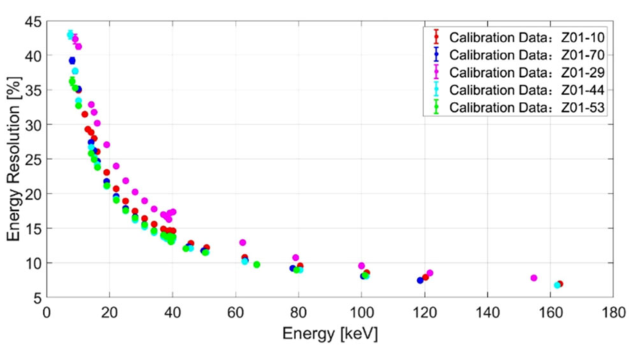


Fig. 22 (Color online) E-FWHM relations of GRDs

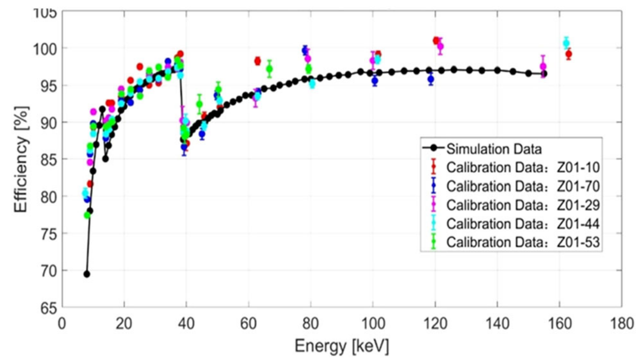


Fig. 23 (Color online) Calibrated detection efficiency of some GRD detectors and MC simulation results

GECAM was launched in 2020. Its main load is a GRD detector that can measure photons in the 6 keV–5 MeV energy range. The core of the GRDs is the $LaBr_3$ crystal. Thus far, 67 detectors (including 50 main detectors and 17 backup detectors) have been calibrated on these monochromatic facilities. The energy range covers (6–160) keV. Four of the detectors completed a fine calibration of the absorption edge (energy interval 0.1 keV). The experimental results are shown in Figs. 22 and 23.

In addition to the two satellite projects described above, the HXI, SVOM, and Gamma Ray Integrated Detectors (GRID) will be calibrated in due course. These projects have also undergone several preliminary calibration experiments. Detector research has also been conducted on these facilities, such as the calibration of a CdTe detector X-ray CCD detector.

## 5 Conclusion

Monochromatic X-ray facilities predicated on the X-ray tube and diffraction were introduced, and their detailed parameters were evaluated. The standard detectors were constructed through Monte Carlo simulations and experiments with a radioactive source with known activity. The (0.218–1.6) keV monochromatic X-ray beam facility was realized in a vacuum environment. Monochromatic X-rays have good monochromaticity and stability in the measurable energy range. The energy range was still relatively narrow and limited by the structure of the device. It was observed that an improved grating support structure or the use of a Bragg diffraction crystal to replace the grating could achieve (1–10) keV X-rays. For (5–301) keV energy range, several measurement and improvement studies have been conducted to provide stable detector testing and calibration services. The results show that there is a linear relationship between flux stability and the X-ray tube current. The experimental results also implied that the performance of the facilities was stable.

In the future, we will broaden the energy range to include both higher and lower energy as part of more detailed research on monochromatic X-ray facilities below 5 keV, to improve the calibration capability of this energy range. Further, attempts will be made to conduct research on new standard detectors such as XTES to create conditions for providing better calibration services. The authors are confident that an internationally renowned monochromatic X-ray calibration base can be built.

**Author contributions** All authors contributed to the study conception and design. Material preparation, data collection and analysis were performed by Si-Ming Guo, Jin-Jie Wu and Dong-Jie Hou. The first draft of the manuscript was written by Si-Ming Guo and all authors commented on previous versions of the manuscript. All authors read and approved the final manuscript.

## References

1. T.P. Li, S.L. Xiong, S.N. Zhang et al., Insight-HXMT observations of the first binary neutron star merger GW170817. Sci. China Phys. Mech. **61**(3), 031011 (2018). https://doi.org/10.1007/s11433-017-9107-5
2. Y.-L. Tuo, M.-Y. Ge, L.-M. Song et al., Insight-HXMT observations of the Crab pulsar. Res. Astron. Astrophys **19**, 087 (2019). https://doi.org/10.1088/1674-4527/19/6/87
3. D. Zhang, X. Li, S. Xiong et al., Energy response of GECAM gamma-ray detector based on LaBr 3: Ce and SiPM array. Nucl. Instrum. Meth. A **921**, 8–13 (2019). https://doi.org/10.1016/j.nima.2018.12.032
4. S. Wang, J.H. Guo, Y. Zhang et al., High-resolution pixelated CdZnTe detector prototype system for solar hard X-ray imager. Nucl. Sci. Tech. **30**, 42 (2019). https://doi.org/10.1007/s41365-019-0571-9
5. D. Gotz, J. Paul, S. Basa et al., SVOM: a new mission for Gamma-ray burst studies. Memorie Della Societa Astronomica Italiana Supplementi **21**(1), 162 (2009). https://doi.org/10.1063/1.3155898
6. Y.W. Dong, B.B. Wu, Y.G. Li et al., SVOM gamma ray monitor. Sci. China Phys. Mech. **53**, 40–42 (2010). https://doi.org/10.1007/s11433-010-0011-7
7. S.N. Zhang, M. Hernanz, A. Santangelo et al. eXTP: Enhanced X-ray Timing and Polarimetry mission. Proceedings Volume 9905, Space Telescopes and Instrumentation 2016: Ultraviolet to Gamma Ray; 99051Q (2017) https://doi.org/10.1117/12.2232034
8. C. Bonnelle, P. Jonnard, J.M. André et al., SOLEX: a tunable monochromatic X-ray source in the 1–20 keV energy range for metrology. Nuclear Instrum. Methods A **516**(2–3), 594–601 (2004). https://doi.org/10.1016/j.nima.2003.09.031
9. M.C. Lépy, L. Ferreux, J. Plagnard, A tunable monochromatic X-ray source for metrological studies in the 1–20 keV energy range: application to the measurement of attenuation coefficients. Appl. Radiat. Isotopes **60**(2–4), 159–165 (2004). https://doi.org/10.1016/j.apradiso.2003.11.010
10. M.C. Lépy, J. Plagnard, Development of low-energy X-ray spectrometry at the Laboratoire National Henri Becquerel. Rev. Mex. Fis. **53**(3), 68–73 (2007)
11. J. Plagnard, M.C. Lépy, Use of tunable monochromatic X-ray sources for metrological studies in the low-energy range at the Laboratoire National Henri Becquerel. International Conference on Nuclear Data for Science and Technology. EDP Sci. 433–436 (2007). https://doi.org/10.1051/ndata:07195
12. A. Collura, M. Barbera, X-ray Astronomy Calibration and Testing Facility (XACT) at Osservatorio Astronomico di Palermo G. S. Vaiana. Proc. SPIE Int. Soc. Opt. Eng. **275**(31), 206–213 (1994). https://doi.org/10.1117/12.186814
13. R.F. Elsner, E.M. Kellogg, B.J. Wargelin, X-ray source system at the Marshall Space Flight Center X-ray calibration facility. Proc. SPIE Int. Soc. Opt. Eng. **2515**, 420–435 (1995). https://doi.org/10.1117/12.212608
14. M.J. Freyberg, H. Bräuninger, W. Burkert et al., The MPE X-ray test facility PANTER: calibration of hard X-ray (15–50 kev) optics. Exp. Astron. **20**(1–3), 405–412 (2005). https://doi.org/10.1007/s10686-006-9068-8
15. F. Frontera, E. Costa, D. Dal Fiume et al., The high energy instrument PDS on-board the BeppoSAX X–ray astronomy satellite. Astron. Astrophys. Suppl. Ser. **122**(2), 357–369 (1997). https://doi.org/10.1051/aas:1997140
16. G. Loffredo, C. Pelliciari, F. Frontera et al., X-ray facility for the ground calibration of the X-ray monitor JEM-X on board INTEGRAL. Astron. Astrophys. **411**(1), L239–L242 (2003). https://doi.org/10.1051/0004-6361:20031402
17. S.S. Murray, A.T. Kenter, R.P. Kraft et al., AXAF high-resolution camera (HRC): calibration and recalibration at XRCF and beyond. Proc Spie **3114**(3), 261–263 (1997). https://doi.org/10.1117/12.283772
18. R. Austin, J. Kolodziejczak, R. Elsner et al., Advanced X-ray Astrophysics Facility (AXAF) – Overview. Space Programs and Technologies Conference. AIAA 95-3746 (2013). https://doi.org/10.2514/6.1995-3746
19. D.N. Burrows, J.E. Hill, J.A. Nousek et al., The swift, X-ray telescope. Space Sci. Rev. **120**(3–4), 165–195 (2005). https://doi.org/10.1007/s11214-005-5097-2
20. E. Bissaldi, A.V. Kienlin, G. Lichti et al., Ground-based calibration and characterization of the Fermi gamma-ray burst monitor detectors. Exp. Astron. **24**(1–3), 47–88 (2009). https://doi.org/10.1007/s10686-008-9135-4
21. X. Zhou, X.Q. Li, Y.N. Xie et al., Introduction to a calibration facility for hard X-ray detectors. Exp. Astron. **38**(3), 433–441 (2014). https://doi.org/10.1007/s10686-014-9393-2
22. T. Pan, R.L. Ni, L. Zhang et al., Insight-HXMT: China's first x-ray astronomical satellite. Aerospace China **18**(4), 3–12 (2017). https://doi.org/10.3969/j.issn.1671-0940.2017.04.001
23. Y. Huang, J.L. Qu, S.N. Zhang et al., Insight-HXMT observations of the new black hole candidate MAXI J1535–571: timing analysis. Astrophys. J. **866**, 122 (2018). https://doi.org/10.3847/1538-4357/aade4c
24. L.R.B. Elton, X-ray diffraction and the Bragg law. Am. J. Phys. **34**(11), 1036 (1966). https://doi.org/10.1119/1.1972439
25. H.R. Liu, J.J. Wu, J.C. Liang et al., LEGe detector intrinsic efficiency calibration for parallel incident photons. Appl. Radiat. Isotopes **109**, 551–554 (2016). https://doi.org/10.1016/j.apradiso.2015.11.102
26. M.C. Lépy, A. Pearce, O. Sima, Uncertainties in gamma-ray spectrometry. Metrologia **52**(3), S123–S145 (2015). https://doi.org/10.1088/0026-1394/52/3/S123
27. X.F. Li, C.Z. Liu, Z. Chang et al., Ground-based calibration and characterization of the HE detectors for Insight-HXMT. J. High Energy Astrophysics **24**, 6–14 (2019). https://doi.org/10.1016/j.jheap.2019.09.003